doi: 10.1093/pasj/xxx000

Image Stacking Analysis of SDSS Galaxies with AKARI Far-Infrared Surveyor Maps at 65μm, 90μm, and 140μm

Taizo OKABE[1], Toshiya KASHIWAGI[1], Yasushi SUTO[1,2], Shuji MATSUURA[3,4], Yasuo DOI[5], Satoshi TAKITA[3] and Takafumi OOTSUBO[5],

[1]Department of Physics, The University of Tokyo, Tokyo 113-0033
[2]Research Center for the Early Universe, School of Science, The University of Tokyo, Tokyo 113-0033
[3]Institute of Space and Astronautical Science, Japan Aerospace Exploration Agency, Kanagawa 252-5210
[4]present address: Department of Physics, School of Science and Technology, Kwansei Gakuin University 2-1 Gakuen, Sanda, Hyogo 669-1337, Japan
[5]Department of Earth Science and Astronomy, Graduate School of Arts and Science, The University of Tokyo, Tokyo 153-8902

*E-mail: taizo.okabe@utap.phys.s.u-tokyo.ac.jp

Received ; Accepted

Abstract

We perform image stacking analysis of Sloan Digital Sky Survey (SDSS) photometric galaxies over the AKARI Far-Infrared Surveyor (FIS) maps at 65μm, 90μm, and 140μm. The resulting image profiles are decomposed into the central galaxy component (single term) and the nearby galaxy component (clustering term), as a function of the r-band magnitude, m_r of the central galaxy. We find that the mean far-infrared (FIR) flux of a galaxy with magnitude m_r is well fitted with $f^s_{90\mu\mathrm{m}} = 13 \times 10^{0.306(18-m_r)}$[mJy]. The FIR amplitude of the clustering term is consistent with that expected from the angular-correlation function of the SDSS galaxies, but galaxy morphology dependence needs to be taken into account for a more quantitative conclusion. We also fit the spectral energy distribution of stacked galaxies at 65μm, 90μm, and 140μm, and derive a mean dust temperature of ~ 30K. This is consistent with the typical dust temperature of galaxies that are FIR luminous and individually detected.

1 Introduction

Dust plays an important role in formation and chemical evolution of galaxies. Dust absorbs and scatters the ultraviolet (UV) light associated with star formation activities, and approximately re-emits half of the star light in infrared (IR) (e.g. Lutz 2014). The infrared dust emission from individual galaxies, however, is very difficult to detect in IR generally, except for bright sources. This is why image stacking analysis is very useful in measuring and characterizing the IR emission from typical galaxies in a statistical fashion.

Recently, for instance, Kashiwagi, Yahata, & Suto. (2013) (hereafter KYS13) performed the stacking analysis of SDSS (York et al. 2000) photometric galaxies over the Galactic extinction map by Schlegel, Finkbeiner, and Davis (Schlegel, et al. 1998, hereafter SFD). The SFD extinction map is constructed basically from IRAS/ISSA FIR emission map at 100μm with dust temperature

correction using the COBE data.

KYS13 were originally motivated to explain the anomaly of the SFD extinction map (Yahata et al. 2007; Kashiwagi et al. 2015) in terms of the FIR emission contamination from galaxies. Indeed they are successful in detecting the additional extinction statistically over the SFD map that should be ascribed to SDSS galaxies. Any further quantitative interpretation of the result, however, is limited by the poor angular resolution (FWHM $\sim 6'$) of the IRAS 100μm map.

In this paper, we perform the similar stacking analysis using the Far-Infrared Surveyor (FIS; Doi et al. 2015, Takita et al. 2015) onboard the Japanese infrared satellite AKARI (Murakami et al. 2007). FIS covers almost 98% of the whole sky with spatial resolution of $\sim 1'.5$, approximately four times better than that of IRAS. Also FIS maps at 65, 90, 140 and 160μm are useful in estimating the corresponding dust temperature in a statistical fashion. Indeed the longer wavelength bands correspond to the peak of dust far-infrared emission from SDSS photometric galaxies as described below.

The present paper is organized as follows. Section 2 briefly summarizes the AKARI FIS all-sky map and SDSS DR7 photometric galaxy catalog that we use throughout the current analysis. Section 3 describes the point spread functions (PSFs) of FIS, and also presents the method of the stacking. The stacked images at 90μm are fitted to the model profiles in section 4, compared with the prediction on the basis of the angular-correlation function of SDSS galaxies in section 5. We repeat the similar stacking analysis at 65 and 140μm, and derive the dust temperature of SDSS galaxies in section 6. Finally §7 is devoted to summary and conclusion of the paper.

2 Data : SDSS and AKARI FIS

Our stacking analysis utilizes the two datasets, AKARI FIS (Kawada et al. 2007) and SDSS DR7 data (Abazajian et al. 2009), which we describe briefly below.

2.1 AKARI FIS All-Sky Maps

FIS is an instrument on board the AKARI satellite (Kawada et al. 2007). It has 4 photometric bands at 65 μm, 90 μm, 140 μm and 160 μm, and covers almost all the sky. Figure 1 shows the 90μm image of FIS map in the ecliptic coordinates. The absolute calibration of FIS map is based on the comparison with the COBE/DIRBE data (Takita et al. 2015). While other component and point sources are not removed, smooth cloud components of the zodiacal emission are subtracted from the map following Gorjian, Wright, & Chary (2000). Indeed, a faint signature of the residual zodiacal light is visible around the equator in figure 1.

The point-source detection levels of the survey mode at a signal-to-noise ratio of 5σ are 2.4Jy, 0.55Jy, and 1.4Jy at 65 μm, 90 μm and 140 μm, respectively (Kawada et al. 2007). Arimatsu et al. (2014) directly measure the point spread functions (PSFs) of FIS by stacking infrared standard stars of Cohen et al. (1999). Their catalogue includes 422 giant stars with spectral types of K0 to M0, and Arimatsu et al. (2014) stack 80% of those stars. Table 1 summarizes the values of the PSFs of FIS and the 5σ detection limits in each wavelength. The PSFs of FIS are elongated along the direction of scanning because of the slow response of FIS detector. This is why we show three different values for the FWHM in Table 1; along the scan direction (In-scan), perpendicular to the scan direction (Cross-scan), and their circular average. Since the 160μm data are too noisy, we do not use them (cf. Arimatsu et al. 2014).

Table 1. The FWHMs of the PSFs of AKARI FIS (Table 2 of Arimatsu et al. 2014) and the 5σ detection limits in each wavelength.

	65μm	90μm	140μm
In-scan FWHM	$82''$	$98''$	$101''$
Cross-scan FWHM	$33''$	$55''$	$70''$
Circular average FWHM	$53''$	$73''$	$86''$
5σ detection limit	2.4Jy	0.55Jy	1.4Jy

2.2 SDSS DR7 Photometric Galaxies

Our stacking analysis is based on the SDSS DR7 (Abazajian et al. 2009) photometric galaxy catalog, which covers 11663 deg^2 of the sky, with photometry in five passbands: $u, g, r, i,$ and z. (See Stoughton et al. 2002; Gunn et al. 1998, 2006; Fukugita et al. 1996; Hogg et al. 2001; Ivezić et al. 2004; Smith et al. 2002; Tucker et al. 2006; Padmanabhan et al. 2008; Pier et al. 2003 for more details

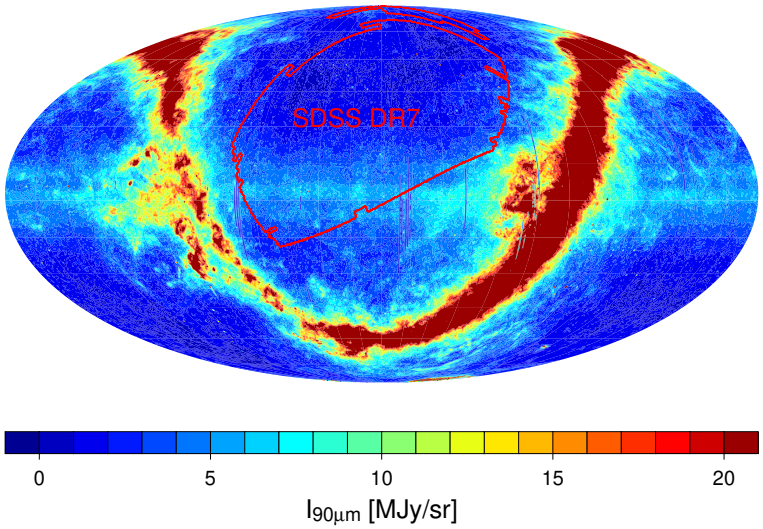

Fig. 1. All-sky map of 90μm observed by AKARI in ecliptic coordinate. The color scale indicates the intensity of FIR emission at 90μm. The region surrounded by the red solid line indicates the SDSS DR7 survey region used in the worth Galactic map for the present analysis.

of photometric data.) We use the contiguous regions of 7270 deg^2 in the north galactic hemisphere (shown in figure 1). We exclude the masked regions so as to avoid those objects with unreliable photometry.

Since the spatial distribution of the Galactic stars is likely to be correlated with that of the Galactic dust, the contamination of stars in our galaxy sample would affect the interpretation of the stacking analysis presented below. Therefore, for ensuring the reliable star-galaxy separation, we conservatively remove bad photometry data and fast-moving objects from the "GALAXY" sample on the basis of the SDSS photometry flag; see Yahata et al. 2007 for more details of our galaxy sample selection.

Finally, we restrict the magnitude range of our galaxy sample as $15.5 < m_r < 20.5$. This is because the star-galaxy separation by the SDSS photometry pipeline works well for those objects with $m_r < 21$ (Yasuda et al. 2001). Our sample selection mentioned above removes 24-39% of the photometric galaxy candidates in each magnitude bin (table 2).

3 Method of Stacking Analysis

3.1 Point Spread Function

Since the PSFs of AKARI FIS are much larger than the typical size of SDSS galaxies, each single galaxy on the stacked image is approximated by the PSFs. Therefore, it is crucially important to model the PSFs accurately. In reality, while the PSFs of AKARI FIS are elongated along the scan directions which align with ecliptic longitudes, we use their circular averages in the following analysis just for simplicity. Since Arimatsu et al. (2014) do not find any systematic dependence of the PSFs on the fluxes of the sources, we ignore the dependence on the source flux and adopt the same PSF independently of m_r of galaxies.

Figure 2 shows the radial profiles of the circular-averaged PSFs. The quoted error-bars represent rms in each radial bin. The relatively large rms comes from the anisotropy of the PSFs. Clearly the circular averaged PSFs have a long tail and are not simply approximated by a single Gaussian (green dashed lines). Instead, we find that the following double Gaussian is a good approximation for the PSFs:

$$W_2(\theta) = A \exp\left(-\frac{\theta^2}{2\sigma_1^2}\right) + (1-A)\exp\left(-\frac{\theta^2}{2\sigma_2^2}\right). \quad (1)$$

We fit equation (1) to the circular averaged PSFs (figure 2) with the three parameters; σ_1, σ_2 and A. The fit is performed for $\theta < 3'$ at 65μm and 90μm, and for $\theta < 2.'4$ at 140μm because of the large error bars beyond these scales. Table 3 lists the best-fit parameters that correspond to the black solid lines in figure 2.

3.2 Stacking Method

Since the detection limits of SDSS are much deeper than those of FIS, the majority of the SDSS galaxies cannot be individually resolved in the FIS maps. The stacking analysis on the FIS maps, however, enables us to statistically measure the average FIR

Table 2. The number of SDSS galaxies used for the stacking analysis, and removed by masking the panels with $I_{90\mu\mathrm{m}} > 200$[MJy/sr] for different r-band magnitudes.

m_r	GALAXY	selected	stacked	removed
$15.5-16.0$	56183	34322	34315	7
$16.0-16.5$	100414	61392	61383	9
$16.5-17.0$	171767	108553	108514	39
$17.0-17.5$	291599	194546	194490	56
$17.5-18.0$	499741	345168	345078	90
$18.0-18.5$	861461	617291	617126	165
$18.5-19.0$	1476678	1099475	1099154	321
$19.0-19.5$	2511481	1909836	1909289	547
$19.5-20.0$	4208480	3179658	3178776	882
$20.0-20.5$	6945931	5042565	5041111	1454

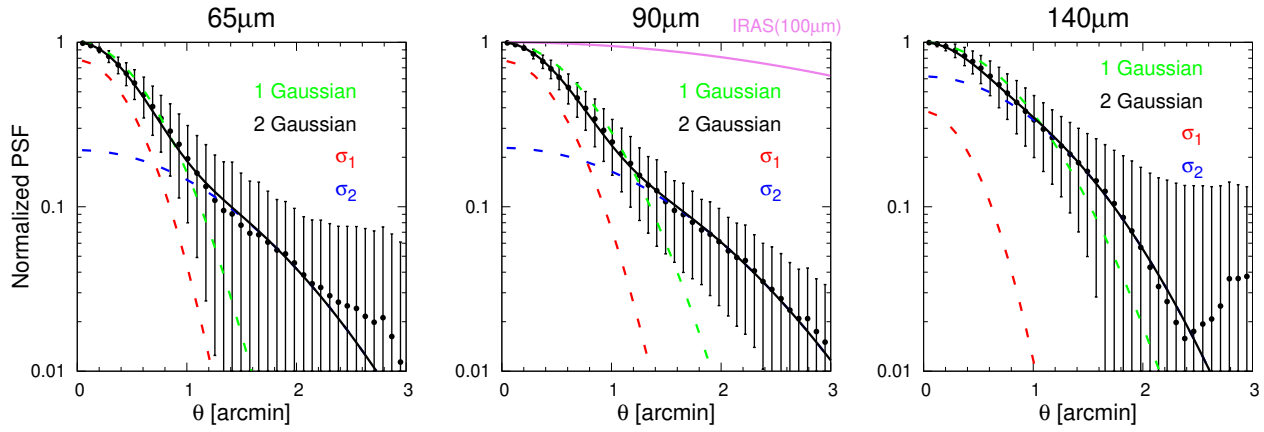

Fig. 2. Circular-averaged PSFs at 65μm (left), 90μm (center), and 140μm (right). The symbols indicate the PSFs measured by Arimatsu et al. (2014). The quoted error-bars represents rms in each circular bin. The green dashed line and black solid line indicate best-fits of single Gaussian and double Gaussian, respectively. The red and blue dashed line correspond to two components of double Gaussian. The violet solid line in the middle panel represents the PSF of IRAS (100μm).

emission of the SDSS galaxies. Our method for the stacking analysis is basically the same as that adopted by KYS13, except for that we mask several bright objects and subtract the zodiacal and Galactic foreground as will be described below.

Consider first the 90μm data. We divide the entire sample of SDSS galaxies according to their r-band magnitude and stack $20' \times 20'$ images of the FIS map centered at the positions of SDSS galaxies in each magnitude bin. In this procedure, we evaluate the value of $I_{90\mu\mathrm{m}}$ on $6'' \times 6''$ pixels over the $20' \times 20'$ images, adopting a cloud-in-cell linear interpolation of the four nearest neighbors in the $15'' \times 15''$ pixels of the original FIS data. We first stack those images fixing the y-direction to the ecliptic longitudes so as to retain the anisotropic PSF of the FIS. Since the FIS map does not remove point sources unlike the SFD data, we exclude those images that contain pixels with $I_{90\mu\mathrm{m}} > 200\mathrm{MJy/sr}$ to avoid the contamination due to bright point sources. We confirmed that our main result does not change even when we adopt $I_{90\mu\mathrm{m}} > 100\mathrm{MJy/sr}$ or $I_{90\mu\mathrm{m}} > 1000\mathrm{MJy/sr}$. Our criterion excludes several large nearby galaxies, and effectively masks about 2 deg^2 in total. Table 2 lists the number of SDSS galaxies labelled as "GALAXY", selected as our sample, and stacked after removing the regions with bright sources.

Figure 3 illustrates our stacking procedure in three different magnitude bins as an example. The left panels indicate the raw stacked results before circular averaging. In addition to the elongated source images, there is a systematic large-scale gradient along the y-axis, which originate from Galactic dust, and residual zodiacal light.

In order to remove the gradient component, we shift the centers of the images by $+20''$ and $-20''$ along the x-axis, *i.e.,* constant ecliptic latitude, from the source galaxy position, and repeat the same stacking. The average of those off-source images (central panels) is used as templates of the Galactic and zodiacal foreground, and is subtracted from the corresponding raw stacked images (left panels).

The right panels of figure 3 show the stacked images after the subtraction. Clearly the large-scale gradient is successfully

Table 3. Best fit parameters of the PSF at each passband of FIS.

	65μm	90μm	140μm
A	0.78	0.77	0.38
σ_1	$25''.0$	$27''.7$	$22''.7$
σ_2	$65''.8$	$73''.8$	$54''.5$

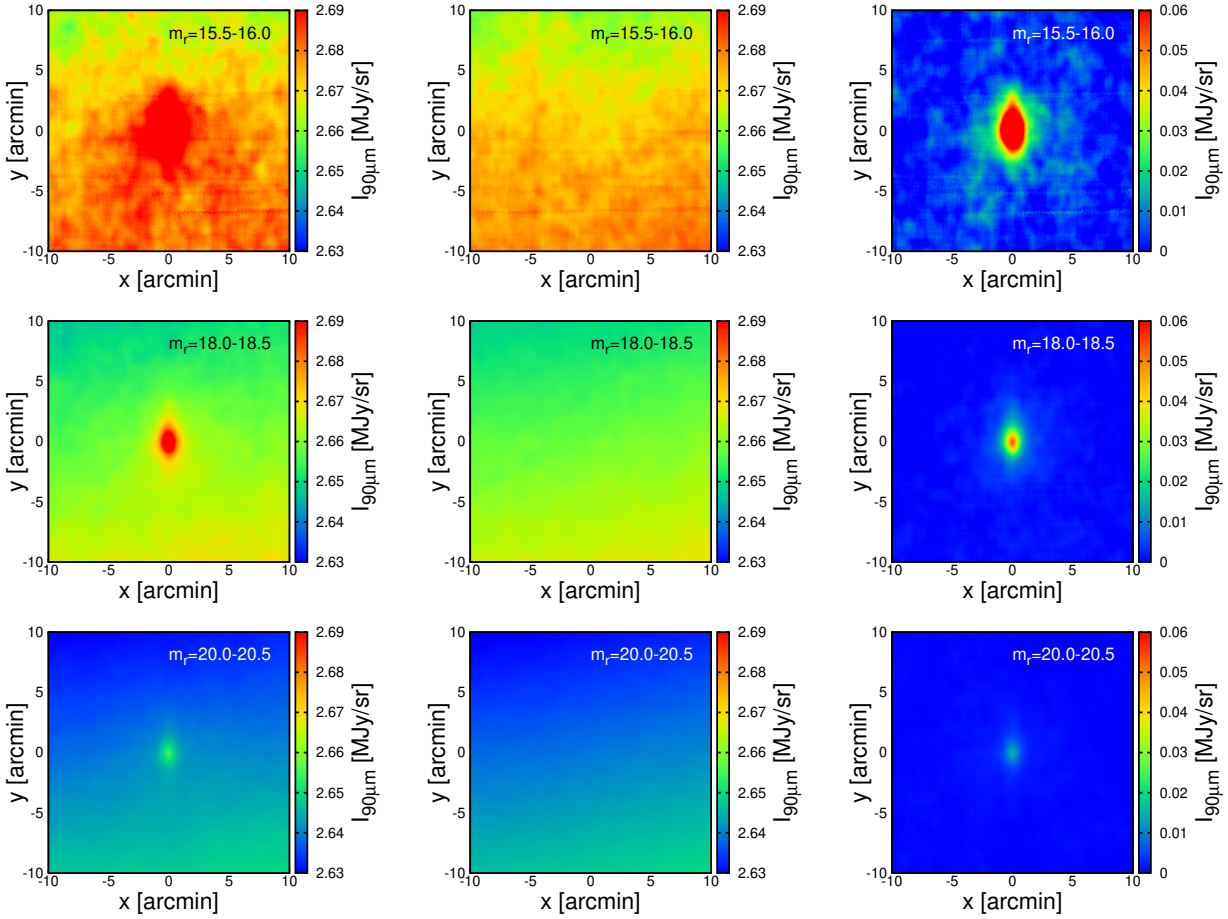

Fig. 3. Left, middle and right panels correspond to the raw stacked images, foreground templates, and the stacked images subtracting the foreground templates, respectively. The upper, center, and lower panels represent the result for $m_r = 15.5$-16.0, 18.0-18.5, and 20.0-20.5, respectively.

removed, and the signal of SDSS galaxies becomes more pronounced; note the different range of $I_{90\mu\mathrm{m}}$ shown in the right color scales. All the analysis below is based on the stacked images corresponding to the right panels of figure 3.

4 Decomposing Stacked Images

Figure 4 displays the stacked images of the SDSS galaxies according to the method described in §3.2 for ten different r-band magnitudes (Table 2). For reference, we show the stacked image of bright stars (bottom middle panel) that should correspond to the PSF of FIS, and the stacked image on IRAS (bottom right panel) as well for comparison. The resulting stacked images exhibit prominent signatures of emission associated with the SDSS galaxies located at the origin, and indicate clearly that the angular resolution of FIS is much better than that of IRAS.

When a typical galaxy of a radius 10kpc is located at the median redshift of the SDSS sample ($\langle z \rangle = 0.36$, Dodelson et al. 2002), the angular size is about $2''$, much smaller than the size of PSFs of FIS. Thus we neglect the intrinsic size of galaxies, which is justified even visually from the comparison between the stacked galaxy and star images (figure 4).

To quantitatively characterize the FIR emission of SDSS galaxies, we compute the circular-averaged radial profiles of the stacked

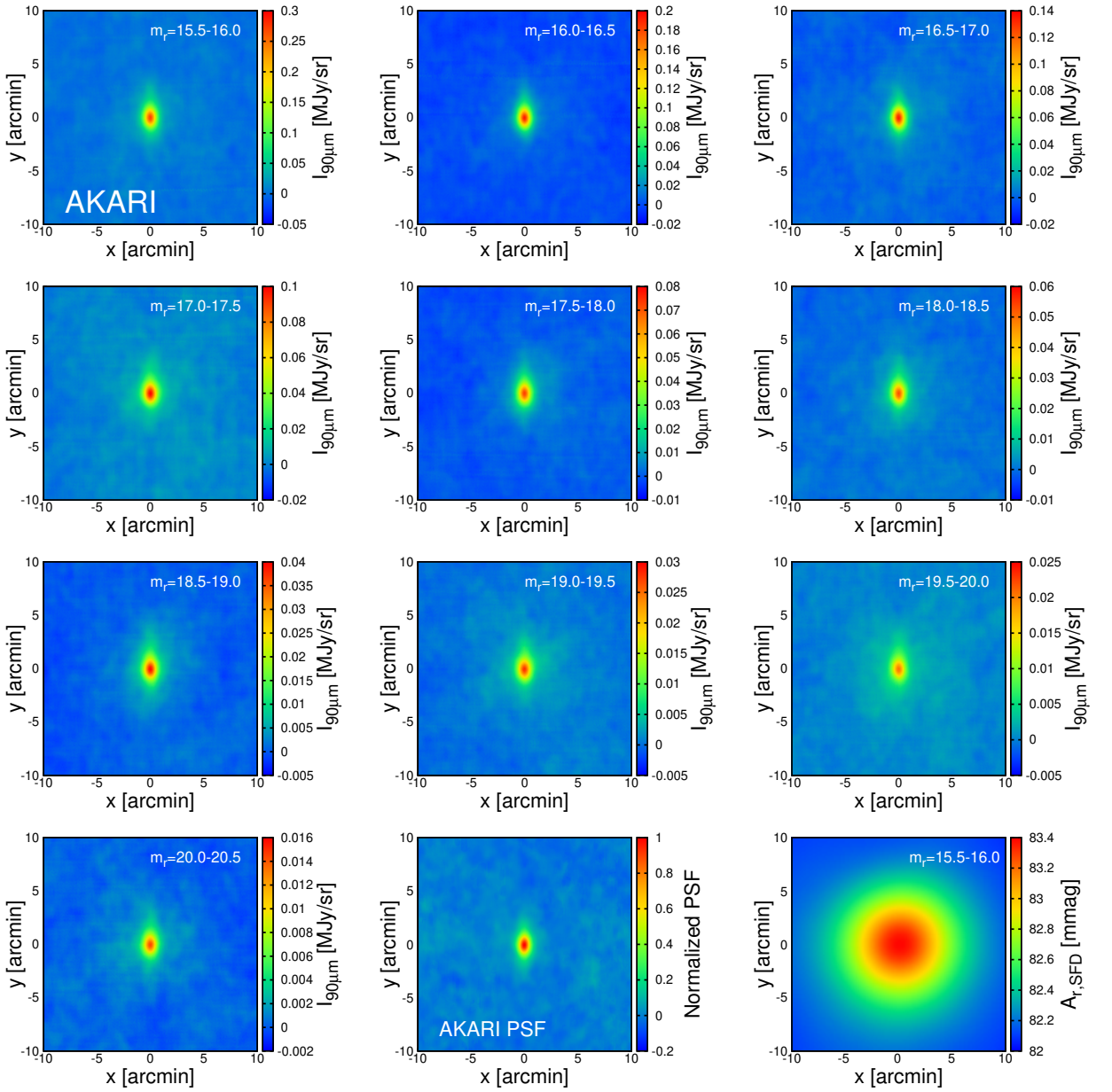

Fig. 4. Stacked images of the AKARI FIS map for $20' \times 20'$ centered at SDSS galaxies of different r-band magnitudes ($m_r = 15.5$-20.5) in 0.5 magnitude bin. The bottom center panel correspond the PSF of FIS at 90μm by Arimatsu et al. (2014). For comparison, the bottom right panel shows the stacked images of SFD extinction map by KYS13.

images, $\Sigma_{\rm g}^{\rm tot}(\boldsymbol{\theta}; m_r)$, in Figure 5; $15.5 < m_r < 16.0$ (left panel) and $20.0 < m_r < 20.5$ (right panel).

The quoted error-bars represent the rms within each radial bin, $\Delta\theta = 7''.76$, and are dominated by the anisotropy of the PSF. Following KYS13, we then model the measured radial profiles as the sum of three components:

$$\Sigma_{\rm g}^{\rm tot}(\boldsymbol{\theta}; m_r) = \Sigma_{\rm g}^{\rm s}(\boldsymbol{\theta}; m_r) + \Sigma_{\rm g}^{\rm c}(\boldsymbol{\theta}; m_r) + \Delta C(m_r), \tag{2}$$

where $\Sigma_{\rm g}^{\rm s}(\boldsymbol{\theta}; m_r)$ is the single term (the contribution from central galaxies in the stacked images), $\Sigma_{\rm g}^{\rm c}(\boldsymbol{\theta}; m_r)$ is the clustering term (the contribution from clustered galaxies around the central galaxies), and ΔC is the residual offset level of the average foreground emission after subtracting the foreground templates. The specific expression for the single and clustering term will be given in equation (3) and (6), respectively, and the residual offset level will be discussed in detail later this section.

Since we neglect the intrinsic size of galaxies, the single term is represented by the PSF profile, equation (1):

$$\Sigma_{\rm g}^{\rm s}(\boldsymbol{\theta}; m_r) = \Sigma_{\rm g}^{\rm s0}(m_r) W_2(\theta). \tag{3}$$

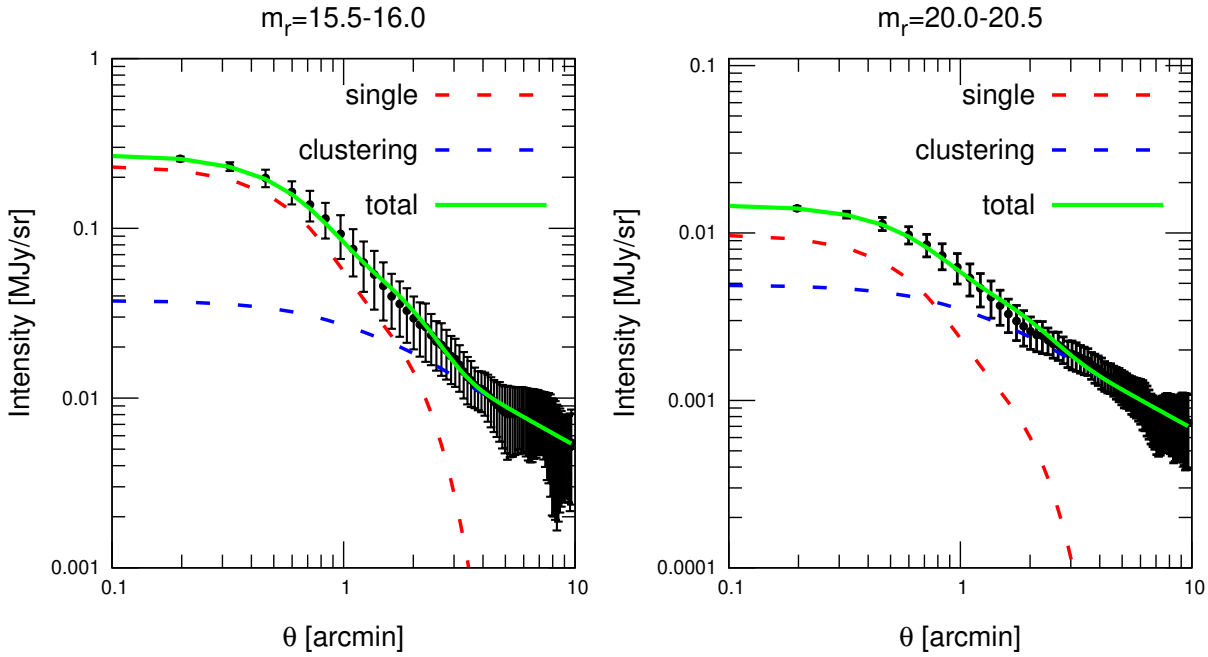

Fig. 5. Circular-averaged radial profiles of the stacked images of SDSS galaxies corresponding to figure 4. Green solid, red, and blue dashed curves indicate the best-fit model of equations (2), (3), and (6), respectively. The quoted error-bars indicate the rms within each radial bin.

Then the clustering term is written as:

$$\Sigma_{\rm g}^{\rm c}(\boldsymbol{\theta};m_r) = \iint dm' d\boldsymbol{\varphi}\, \Sigma_{\rm g}^{\rm s}(\boldsymbol{\theta}-\boldsymbol{\varphi};m') w_{\rm g}(\boldsymbol{\varphi};m',m_r) n_{\rm g}(m'), \tag{4}$$

where $w_{\rm g}(\boldsymbol{\varphi};m',m_r)$ is the angular correlation function of galaxies with magnitude m' located at $\boldsymbol{\varphi}$ from the central galaxy with magnitude m_r, and $n_{\rm g}(m') \equiv dN_{\rm g}(m')/dm'$ is the differential galaxy number density.

These two functions are directly measured from the SDSS galaxies; figure 6 plots the differential galaxy number density, and figure 7 shows the angular-correlation function of SDSS galaxies for $m' = m_r$. We also find that the angular-correlation function for $m' \neq m_r$ obeys the same power-law, and can be approximated as

$$w_{\rm g}(\boldsymbol{\varphi};m',m_r) = K(m',m_r)\left(\frac{\varphi}{\varphi_0}\right)^{-\gamma}, \tag{5}$$

with γ and φ_0 being independent of m_r. We adopt $\gamma = 0.75$, which is confirmed to be valid for $\varphi < 1^\circ$ (Connolly et al. 2002; Scranton et al. 2002). For reference, the dashed line in figure 7 shows $\gamma = 0.75$.

Substituting equations (3) and (5) into equation (4) yields

$$\Sigma_{\rm g}^{\rm c}(\boldsymbol{\theta};m_r) = \Sigma_{\rm g}^{\rm c0}(m_r) W^{\rm c}(\theta), \tag{6}$$

$$\Sigma_{\rm g}^{\rm c0}(m_r) = 2\pi\left(A\sigma_1^{2-\gamma} + (1-A)\sigma_2^{2-\gamma}\right)\left(\frac{\varphi_0}{\sqrt{2}}\right)^{\gamma}\Gamma\left(1-\frac{\gamma}{2}\right)\int dm' \Sigma_{\rm g}^{\rm s0}(m') K(m',m_r) n_{\rm g}(m'), \tag{7}$$

$$W^{\rm c}(\theta) \equiv B\exp\left(-\frac{\theta^2}{2\sigma_1^2}\right){}_1F_1\left(1-\frac{\gamma}{2};1;\frac{\theta^2}{2\sigma_1^2}\right) + (1-B)\exp\left(-\frac{\theta^2}{2\sigma_2^2}\right){}_1F_1\left(1-\frac{\gamma}{2};1;\frac{\theta^2}{2\sigma_2^2}\right), \tag{8}$$

where ${}_1F_1\left(\alpha;\beta;x\right)$ is a confluent hypergeometric function, and

$$B \equiv \frac{A\sigma_1^{2-\gamma}}{A\sigma_1^{2-\gamma} + (1-A)\sigma_2^{2-\gamma}}. \tag{9}$$

In this section, we do not use equation (7), and fit equations (2), (3), (6), and (8) to the observed circular-averaged radial profiles of the stacked images separately for each magnitude by varying the three parameters $\Sigma_{\rm g}^{\rm s0}(m_r)$, $\Sigma_{\rm g}^{\rm s0}(m_r)$, and $\Delta C(m_r)$. The comparison of the resulting $\Sigma_{\rm g}^{\rm c0}(m_r)$ with equation (7) will be considered in the next section.

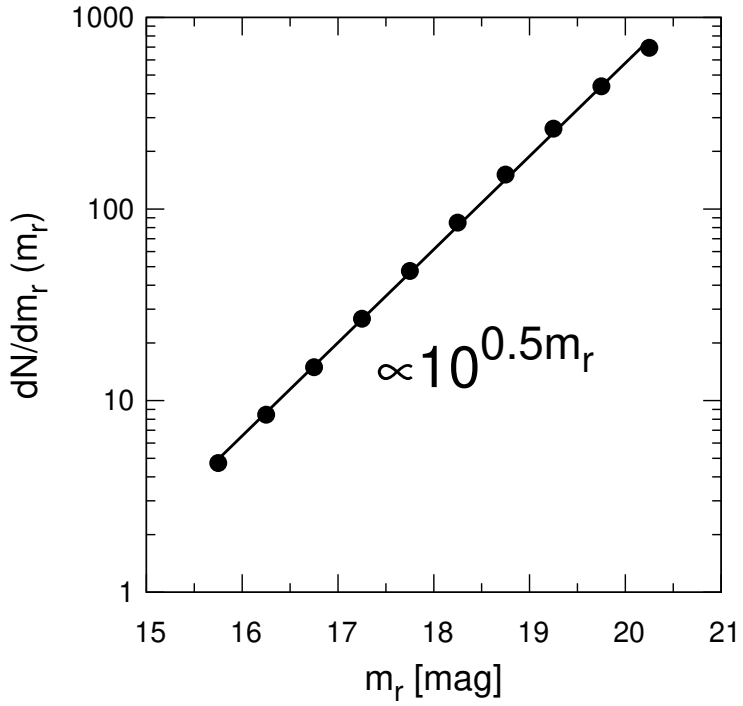

Fig. 6. Differential number count of the SDSS galaxies as a functional of r-band magnitudes. The symbols and solid line show the SDSS data and their best-fit, respectively.

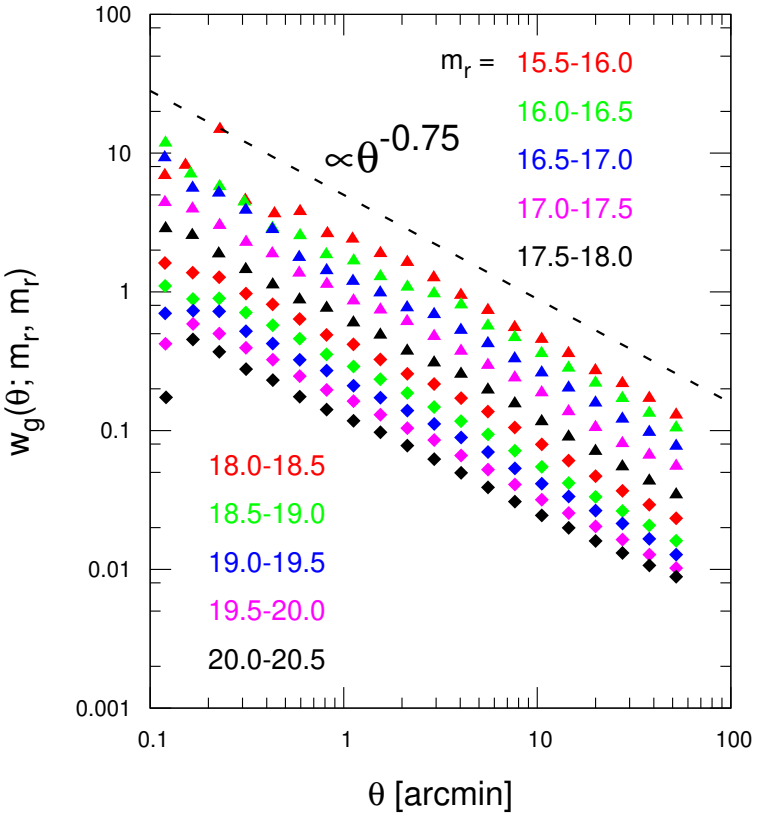

Fig. 7. The angular-correlation function of SDSS galaxies for each magnitude bin. The black dashed line indicates $\gamma = 0.75$.

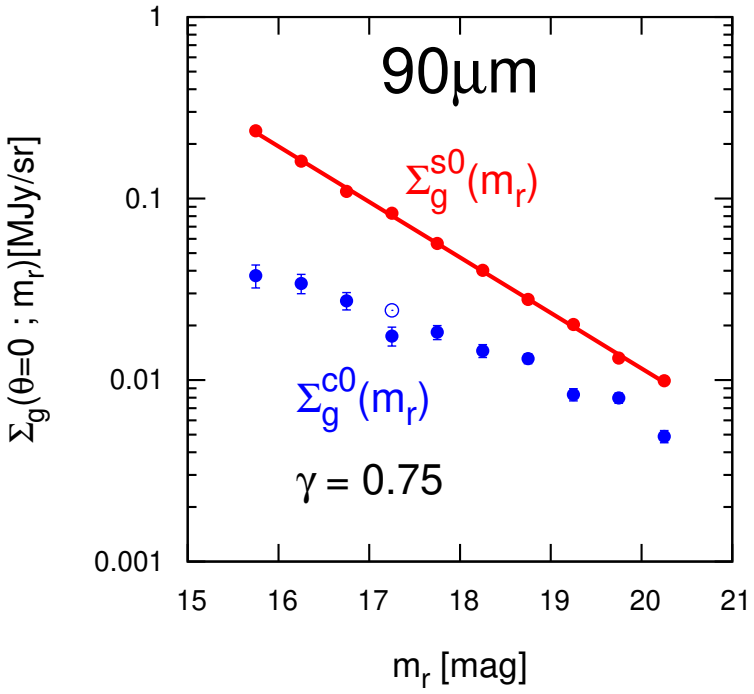

Fig. 8. Best-fit parameters characterizing the FIR emission of galaxies against their r-band magnitude. The quoted error-bars are computed from 1000 subsamples of jackknife resampling. Red and blue solid symbols indicate the best-fit values of $\Sigma_{\rm g}^{\rm s0}(m_r)$, and $\Sigma_{\rm g}^{\rm c0}(m_r)$, respectively, assuming $\gamma = 0.75$. The red solid line indicates to the best-fit line of the best-fit value of $\Sigma_{\rm g}^{\rm s0}(m_r)$ corresponding to the equation (17).

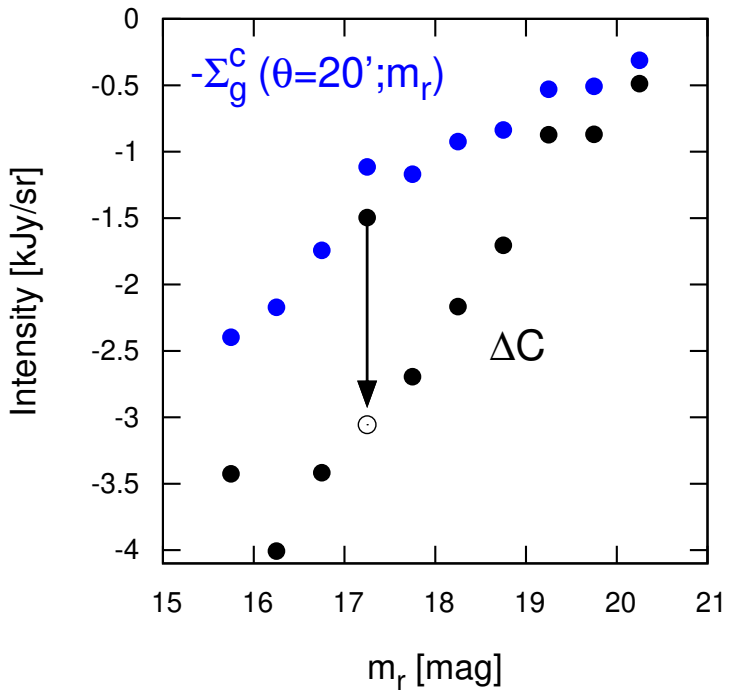

Fig. 9. Best-fit parameters of residual constant term against their r-band magnitude (black solid symbols) and negative value of clustering term at $\theta = 20'$, $-\Sigma_{\rm g}^{\rm c}(\theta = 20'; m_r)$ (blue solid symbols).

The resulting best-fits are plotted in green solid, red dashed, and blue dashed curves, respectively, in figure 5. Figure 8 shows the best-fits of $\Sigma_{\rm g}^{\rm s0}(m_r)$ and $\Sigma_{\rm g}^{\rm c0}(m_r)$ against m_r, where the quoted error-bars are computed from 1000 subsamples of the jackknife resampling method. The results indicate that the single term dominates the clustering term around the center of the stacked images. This is in marked contrast to the result of KYS13 for IRAS at 100μm; their figures 8, 9 and 10 indicate that $\Sigma_{\rm g}^{\rm c0}(m_r)$ is significantly larger than $\Sigma_{\rm g}^{\rm s0}(m_r)$. Thanks to the better angular resolution of AKARI, we are able to separate the prominent emission from the central galaxy from the surrounding diffuse component due to the nearby galaxies. This also implies that the AKARI data enable us to measure the contribution of single term more robustly, in a less model dependent fashion. The difference between AKARI and IRAS will be discussed in detail later in this section.

Figure 9 also indicates that ΔC at $17.0 < m_r < 17.5$ bin significant departs from the systematic trend of the entire samples. A similar gap is also seen for $\Sigma_{\rm g}^{\rm c0}(m_r)$ in figure 8. Indeed, if we use the value of ΔC at $17.0 < m_r < 17.5$ bin from the interpolation of the adjacent bins (black open circle in figure 9), the resulting best-fit of $\Sigma_{\rm g}^{\rm c0}(m_r)$ also matches the other trend (blue open circle in figure 8). While we are not yet able to identify the reason of this behavior, we do not correct for this in the analysis below.

Figure 9 shows that the best-fit values of ΔC systematically increase against m_r. Such m_r-dependence of ΔC seems unphysical, and is likely to result from our foreground (Galactic component) subtraction procedure. Our foreground templates are computed from the stacked images at $\pm 20'$ away from the center, and thus the radial profiles of the foreground-subtracted data should vanish at $\theta = 20'$ even though the clustering term would still extend beyond the scale. As a consequence of the over-correction, we thought that the residual of the foreground ΔC would be equal to $-\Sigma_{\rm g}^{\rm c}(\theta = 20'; m_r)$. As shown in figure 9, however, this does not hold exactly even though the qualitative trend is consistent; the blue and black filled circles differ by a factor of two. We suspect that this difference should come from the difficulty to decompose the weak radial dependence of the clustering term from the constant offset due to the Galactic dust in our model fit. In any case, we made sure that this dependence does not affect our main conclusion, and we do not consider it in what follows.

It is also interesting to compare the present result with that obtained by KYS13 for IRAS. For that purpose, we compute the fluxes of the single galaxy at the center of the stacked map:

$$f^s(m_r;\theta_{\rm max}) = \int \Sigma_{\rm g}^{\rm s}(\boldsymbol{\theta};m_r)d\boldsymbol{\theta} \simeq 2\pi \int_0^{\theta_{\rm max}} \Sigma_{\rm g}^{\rm s0}(m_r)W_2(\theta)\theta d\theta, \tag{10}$$

and the contribution of neighbor galaxies around the center galaxy:

$$f^c(m_r;\theta_{\rm max}) = \int \Sigma_{\rm g}^{\rm c}(\boldsymbol{\theta};m_r)d\boldsymbol{\theta} \simeq 2\pi \int_0^{\theta_{\rm max}} \Sigma_{\rm g}^{\rm c0}(m_r)W^{\rm c}(\theta)\theta d\theta. \tag{11}$$

The integral (11) does not converge for $w(\theta) \propto \theta^{-0.75}$, but the power-law is not valid for $\theta > 1^\circ$ in any way. Thus we introduce an upper limit, $\theta_{\rm max}$, in the integral. Its value is somewhat arbitrary, but we adopt $\theta_{\rm max} = 10'$ because we only use the profiles of stacked images to $\theta = 10'$ for the fitting. Figure 10 shows the flux as a function of $\theta_{\rm max}$ in equations (10) and (11). The left and right panels correspond to $f^{\rm s}(m_r;\theta_{\rm max})$ and $f^{\rm c}(m_r;\theta_{\rm max})$, respectively, for AKARI (red line) and IRAS (blue line). Figure 10 suggests that the fluxes of the single term for both AKARI and IRAS converge at $\theta_{\rm max} \sim 10'$, while the fluxes of the clustering term diverge.

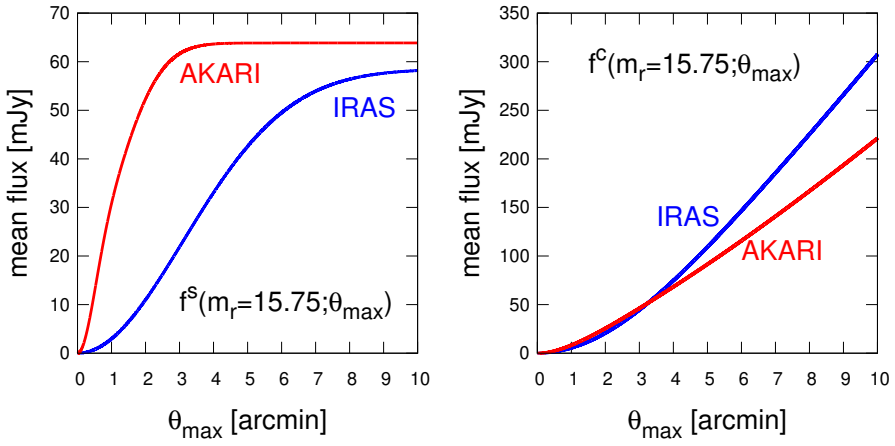

Fig. 10. Flux of galaxies integrated within $\theta_{\rm max}$ for AKARI (red) and IRAS (blue). Left and right panels correspond to the flux of single term and clustering term, respectively.

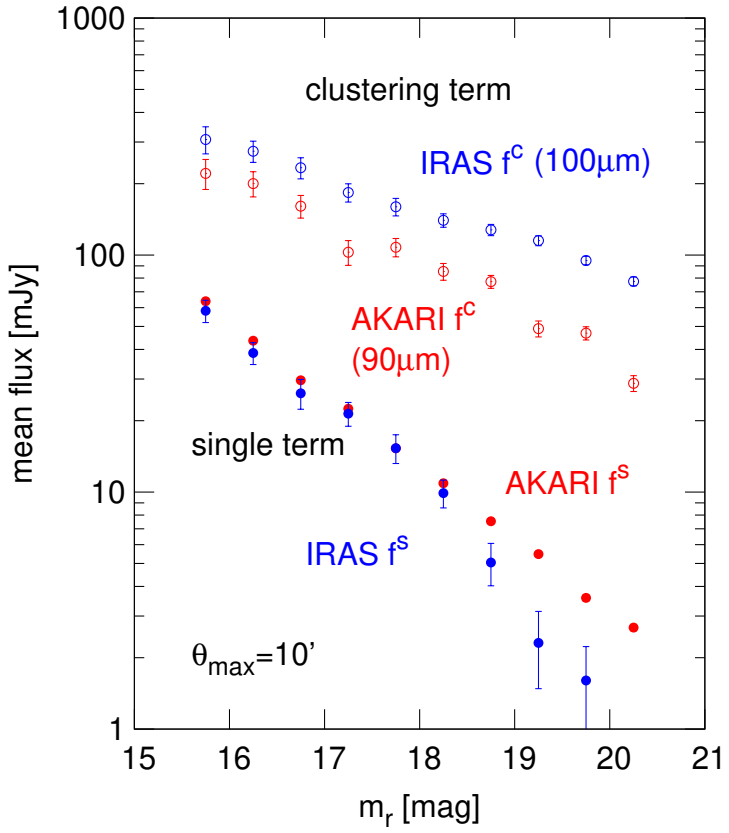

Fig. 11. The flux of galaxies integrated up to $\theta_{\rm max} = 10'$ against their r-band magnitude for AKARI (red) and IRAS (blue). Solid and open symbols indicate the flux corresponding to the single and clustering term, respectively.

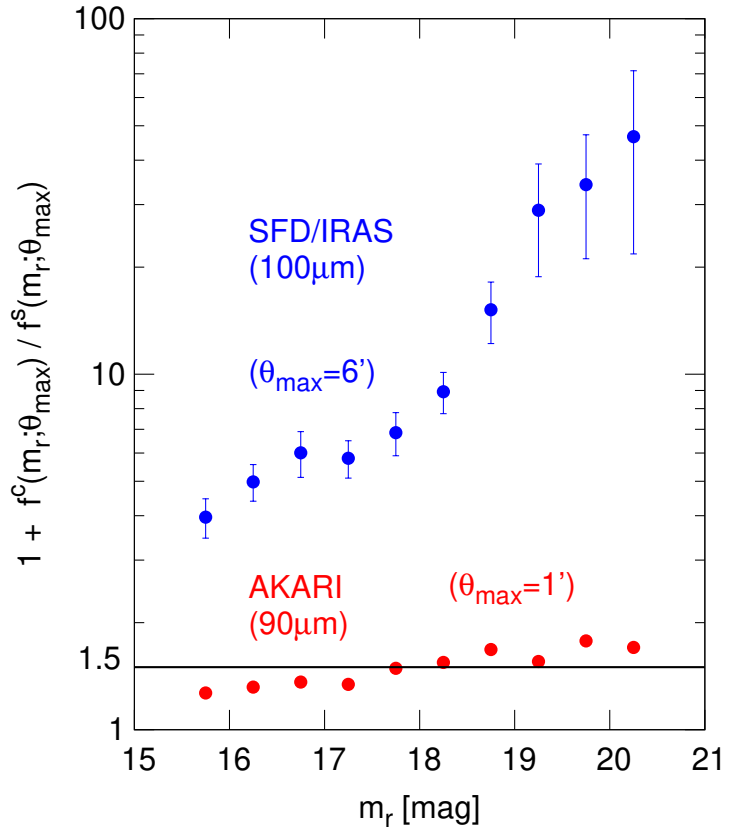

Fig. 12. The ratio of the total flux (=$f^{\rm s} + f^{\rm c}$) to the single flux, $f^{\rm s}$, for both IRAS (blue) and AKARI (red). The ranges of the integral are adopted $\theta_{\rm max} = 1'.0, 6'.0$ for AKARI and IRAS, respectively.

Figure 11 compares the central flux amplitudes for the single and clustering terms ($\theta_{\rm max} = 10'$) estimated from the AKARI and IRAS stacking analysis. The blue and red symbols indicate the fluxes derived from the IRAS (100μm) and AKARI (90μm), respectively. Note that the fluxes of IRAS and AKARI are obtained for different wavelength. For the single term, the fluxes derived from the IRAS and AKARI agree well except for the fainter magnitude samples ($m_r > 18.0$). The resulting mean 90μm flux of a galaxy of m_r is well fitted to

$$f^s_{90\mu{\rm m}} = 13 \times 10^{0.306(18-m_r)}[{\rm mJy}]. \tag{12}$$

On the other hand, the IRAS analysis for the clustering term systematically over-predicts that expected from AKARI. This should be ascribed to the difficulty of the decomposition from the lower angular-resolution data of IRAS. Although the amplitudes of the clustering fluxes depend on $\theta_{\rm max}$, the ratio of fluxes measured by AKARI and IRAS is independent of $\theta_{\rm max}$.

Incidentally, the presence of the clustering term tends to overestimate the flux of a galaxy if not properly decomposed. Figure 12 shows the overestimate factor, $(1 + f^c(m_r;\theta_{\rm max})/f^s(m_r;\theta_{\rm max}))$, against m_r for both the IRAS and AKARI results. Here, we adopt the FWHM of PSF, $1.'0$ for AKARI and $6.'0$ for IRAS, as $\theta_{\rm max}$ for computing the fluxes according to equation (10) and (11). Therefore, this ratio basically indicates to what extent the flux of single galaxy is overestimated, due to the confusion of the fluxes from neighboring galaxies within the angular resolution scales of the PSFs. Thanks to the higher angular-resolution, the overestimation is significantly reduced for AKARI, but still 50% systematic overestimate exist for $m_r > 18$, thus we note that the fluxes of such faint galaxies are potentially overestimated by this level.

Finally, we derive the relative luminosity at frequencies of $\nu_{\rm FIR}$ and ν_r relation between $\nu_{\rm FIR}\langle L_{\rm FIR}\rangle$ and $\nu_r\langle L_r\rangle$, since the r-band magnitude, m_r, and the mean flux, $f^s(m_r)$, should correspond to the same galaxy. Figure13 plots $\nu_{\rm FIR}\langle L_{\rm FIR}\rangle/\nu_r\langle L_r\rangle$ as a function of m_r. The blue, red, and green circles indicate the ratio at 65μm, 90μm, and 140μm, respectively. This ratio monotonically increases as m_r, while KYS13 suggests that this ratio is approximately constant from IRAS data independent of the r-band magnitude (the black symbols in figure13). The differences of m_r dependence of the luminosity ratio should be ascribed to the underestimation of the flux for the fainter galaxies, $m_r > 18.0$ (see figure 11). Indeed, the ratio of IRAS indicates the similar trend of AKARI for the brighter galaxies, $m_r < 18.0$, where the flux estimation is well performed. The ratio of $\nu_{\rm FIR}\langle L_{\rm FIR}\rangle$ to $\nu_r\langle L_r\rangle$ for 90μm is described as follows;

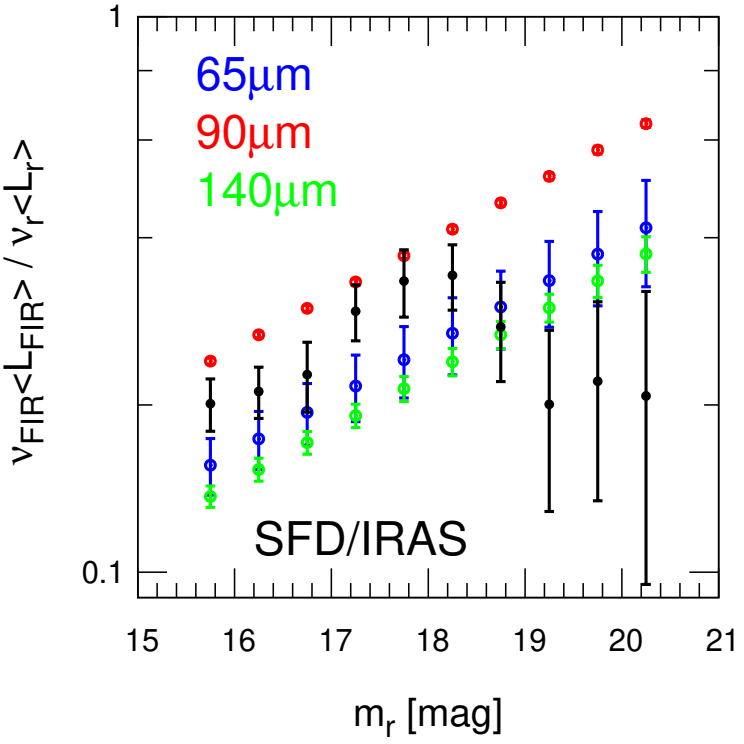

Fig. 13. The relation between far-infrared luminosities of the central galaxy and their r-band luminosities as a function of m_r.

$$\frac{\nu_{\rm FIR}\langle L_{\rm FIR}\rangle}{\nu_r\langle L_r\rangle} = 0.39\times 10^{0.096(m_r-18)}, \tag{13}$$

While this increasing trend may indicate that optically faint galaxies are relatively brighter in far-infrared, we do not discuss the implications here since they are beyond the scope of this paper.

5 Comparison of the clustering term in FIR and the prediction from the angular-correlation function of SDSS galaxies

In the last section, we estimate $\Sigma^{\rm c0}_{\rm g,obs}(m_r)$ from the best-fit to the observed profiles of the stacking images. It is interesting to compare the resulting value to the prediction from equation (7), $\Sigma^{\rm c0}_{\rm g,model}(m_r)$. Indeed KYS13 carried out the comparison and suggested that the FIR fluxes for the clustering term obtained from the IRAS stacking analysis exceed those predicted from the angular-correlation of the SDSS galaxies by a factor of a few. KYS13 speculate that this deficit may point to the existence of unknown FIR objects other than SDSS galaxies.

Since this has very important implications, we repeat the same analysis but with the values estimated from AKARI. As indicated in figure 11, the amplitudes of the clustering term derived from the current AKARI analysis are systematically smaller than those from IRAS. Thus the deficit discovered by KYS13 needs to be examined carefully again.

For this purpose, we first note that equation (7) is written down more explicitly as

$$\Sigma^{\rm c0}_{\rm g,model}(m_r;-\infty<m'<\infty) = 2\pi\left(A\sigma_1^{2-\gamma}+(1-A)\sigma_2^{2-\gamma}\right)\left(\frac{\varphi_0}{\sqrt{2}}\right)^{\gamma}\Gamma\left(1-\frac{\gamma}{2}\right) \times\int_{-\infty}^{\infty} dm'\Sigma^{\rm s0}_{\rm g}(m')K(m',m_r)n_{\rm g}(m'). \tag{14}$$

Since both KYS13 and our work use SDSS galaxies with $m_r = 15.5$-20.5 in the image stacking, we can reliably compute the integral in equation (14) only for $15.5 < m' < 20.5$:

$$\Sigma^{\rm c0}_{\rm g,model}(m_r;15.5<m'<20.5) = 2\pi\left(A\sigma_1^{2-\gamma}+(1-A)\sigma_2^{2-\gamma}\right)\left(\frac{\varphi_0}{\sqrt{2}}\right)^{\gamma}\Gamma\left(1-\frac{\gamma}{2}\right) \times\int_{15.5}^{20.5} dm'\Sigma^{\rm s0}_{\rm g}(m')K(m',m_r)n_{\rm g}(m'). \tag{15}$$

In figure 14, we plot the above result for $\gamma = 0.75$ as a black solid line, which should be compared with $\Sigma^{\rm c0}_{\rm g,obs}(m_r)$ (filled circles with error-bars). Although an overall factor of a few discrepancy in KYS13's analysis (see their figure 10) is significantly reduced, $\Sigma^{\rm c0}_{\rm g,model}(m_r)$ is smaller than $\Sigma^{\rm c0}_{\rm g,obs}(m_r)$ for $m_r < 18$. In this sense, our result is still consistent with that of KYS13.

Nevertheless the deficit may simply come from the upper and lower limits of the integral in equation (15). In order to evaluate equation (14), and we extrapolate the functions $n_{\rm g}(m_r)$, $\Sigma^{\rm s0}_{\rm g}(m_r)$ and $K(m_r,m')$ beyond the magnitude range of the SDSS sample.

For this purpose, we use the observed $n_{\rm g}(m_r)$, $\Sigma^{\rm s0}_{\rm g}(m_r)$ and $K(m_r,m')$ for $15.5 \le m_r \le 20.5$, plotted in figures 6, 8, and 15, and attempt the following power-law fits:

$$n_{\rm g}(m_r) = N\times 10^{\nu m_r}, \tag{16}$$

$$\Sigma^{\rm s0}_{\rm g}(m_r) = S\times 10^{-\mu m_r}, \tag{17}$$

$$K(m_r,m') = K\times 10^{-\alpha(m_r+m')-\beta(m_r-m')^2}. \tag{18}$$

We estimate the constants, α,β,μ,ν, S, N, and K from the least-square fit for $\log K(m_r,m')$, $\log n_{\rm g}(m_r)$ while χ^2 minimizing fit for $\Sigma^{\rm s0}_{\rm g}(m_r)$. The resulting fits are plotted as solid curves in figures 6, 8, and 15.

We evaluate equation (14) assuming that the above extrapolation is valid. Red and blue dashed lines in figure 14 show $\Sigma^{\rm c0}_{\rm g,model}(m_r; m_{r,\rm min}<m'<m_{r,\rm max})$ with $m_{r,\rm min}=10.5$ and $m_{r,\rm max}=20.5$ and 25.5, respectively. The result suggests that $\Sigma^{\rm c0}_{\rm g,model}(m_r)$ sensitively depend on the contribution from galaxies outside the observed magnitude range; $\Sigma^{\rm c0}_{\rm g,model}(m_r=15.5)$ and $\Sigma^{\rm c0}_{\rm g,model}(m_r=20.5)$ are significantly affected by galaxies with $m'<15.5$ and with $m'>20.5$, respectively. We confirmed that $\Sigma^{\rm c0}_{\rm g,model}(m_r)$ for $15.5<m_r<20.5$ is converged if we set $m_{r,\rm min}=10.5$ and $m_{r,\rm max}=25.5$.

Therefore the conclusion of KYS13 that the SDSS galaxies explain less than half of the observed FIR amplitude for the clustering term is most likely due to the magnitude limit of the SDSS galaxies themselves. Indeed if our extrapolation model is correct, the conclusion would be completely opposite; *the observed FIR fluxes are smaller than those predicted from the SDSS galaxies*.

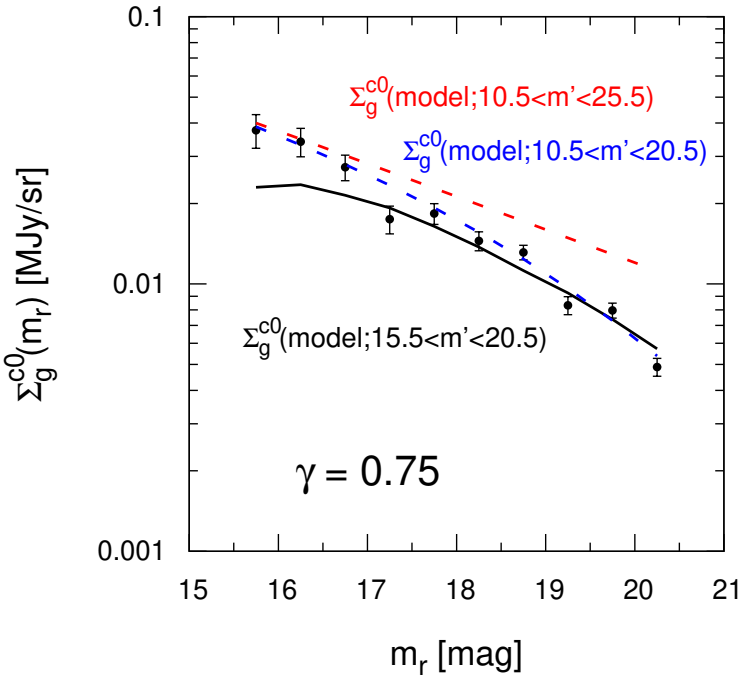

Fig. 14. The values of clustering term against their r-band magnitude. The symbols, blue dashed and red solid line indicate best-fit parameters from fitting, model from SDSS data $m_{r,\min} = 15.5$, $m_{r,\min} = 10.5$, respectively.

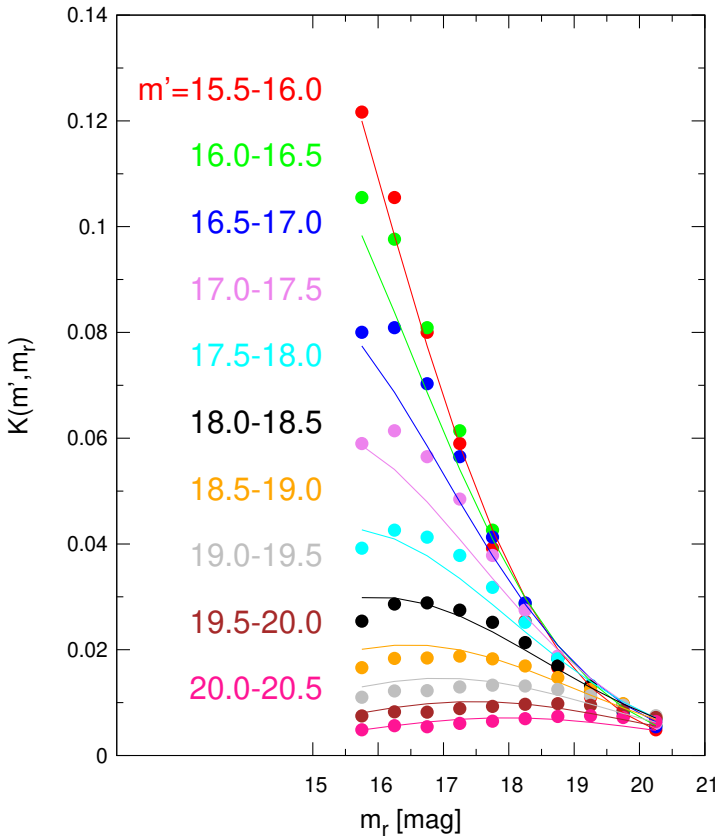

Fig. 15. Amplitudes of the angular-correlation function of SDSS galaxies, $K(m', m_r)$, against m_r. The solid lines indicate the best-fit models of equation (18).

We do not take this possible discrepancy seriously, partly because it is crucially dependent on the extrapolation of the observed angular-correlation function, and also partly because that the galaxy morphology and redshift evolution are totally neglected here. Since dust emission from spirals is stronger than that from ellipticals, the stacking analysis incorporating the morphological dependence is needed to address the above problem properly. We attempt to qualitatively consider the effect of the morphology dependence of $\Sigma^{\rm c0}_{\rm g,model}(m_r)$ below.

Just for simplicity, we assume that galaxies are divided into only two different morphological classes; ellipticals and spirals. We write $n_{\rm g}(m_r) = n_{\rm e}(m_r) + n_{\rm s}(m_r)$, where indexes of the each value e, and s correspond to ellipticals, and spirals, respectively. The angular-correlation functions are assumed to follow the same power-law but with different amplitudes; $w_{\rm ij}(m', m_r) = K_{\rm ij}(m', m_r)(\varphi/\varphi_0)^{-\gamma}$ (i,j=e,s), where $w_{\rm ee}$, $w_{\rm es}$, and $w_{\rm ss}$ denote the angular-correlation functions between ellipticals and ellipticals, ellipticals and spirals, and spirals and spirals, respectively. In addition, we assume that the amplitudes of the angular-correlation functions are related to each other in terms of the constant linear bias factor as

$$\begin{aligned} K_{\rm ee}(m', m_r) &= b_{\rm e}^2 K(m', m_r) \\ K_{\rm es}(m', m_r) &= K_{\rm se}(m', m_r) = b_{\rm e} b_{\rm s} K(m', m_r) \\ K_{\rm ss}(m', m_r) &= b_{\rm s}^2 K(m', m_r). \end{aligned} \tag{19}$$

Then $\Sigma^{\rm c0}_{\rm g,model}(m_r)$ of equation (14) is written as

$$\begin{aligned} \Sigma^{\rm c0}_{\rm g,model}(m_r) = 2\pi \left(A\sigma_1^{2-\gamma} + (1-A)\sigma_2^{2-\gamma}\right) \left(\frac{\varphi_0}{\sqrt{2}}\right)^{\gamma} \Gamma\left(1-\frac{\gamma}{2}\right) \\ \times \int dm' \left(\frac{n_{\rm e}(m')}{n_{\rm g}(m')} \Sigma_{\rm g}^{\rm s0,e}(m') + \frac{n_{\rm s}(m')}{n_{\rm g}(m')} \Sigma_{\rm g}^{\rm s0,s}(m')\right) \times K(m', m_r) n_{\rm g}(m') \\ \times \frac{n_{\rm e}(m') n_{\rm e}(m_r) b_{\rm e}^2 + n_{\rm e}(m') n_{\rm s}(m_r) b_{\rm e} b_{\rm s} + n_{\rm s}(m') n_{\rm e}(m_r) b_{\rm e} b_{\rm s} + n_{\rm s}(m') n_{\rm s}(m_r) b_{\rm s}^2}{n_{\rm g}(m') n_{\rm g}(m_r)}. \end{aligned} \tag{20}$$

On the other hand, the value obtained from the stacking image profile fitting is written as

$$\begin{aligned} \Sigma^{\rm c0}_{\rm g,obs}(m_r) = 2\pi \left(A\sigma_1^{2-\gamma} + (1-A)\sigma_2^{2-\gamma}\right) \left(\frac{\varphi_0}{\sqrt{2}}\right)^{\gamma} \Gamma\left(1-\frac{\gamma}{2}\right) \\ \times \int dm' \left[\frac{n_{\rm e}(m_r)}{n_{\rm g}(m_r)} \left(\Sigma_{\rm g}^{\rm s0,e}(m') b_{\rm e}^2 n_{\rm e}(m') + \Sigma_{\rm g}^{\rm s0,s}(m') b_{\rm e} b_{\rm s} n_{\rm s}(m')\right) \right. \\ \left. + \frac{n_{\rm s}(m_r)}{n_{\rm g}(m_r)} \left(\Sigma_{\rm g}^{\rm s0,s}(m') b_{\rm s}^2 n_{\rm s}(m') + \Sigma_{\rm g}^{\rm s0,e}(m') b_{\rm e} b_{\rm s} n_{\rm e}(m')\right)\right] K(m', m_r). \end{aligned} \tag{21}$$

Therefore the ratio of the integrals in equations (20) and (21) reduce to

$$r \equiv \frac{\Sigma^{\rm c0}_{\rm g,obs}}{\Sigma^{\rm c0}_{\rm g,model}} = \frac{(1 + f_\Sigma f_n f_b)(1 + f_n)}{(1 + f_\Sigma f_n)(1 + f_n f_b)}, \tag{22}$$

where

$$f_\Sigma \equiv \frac{\Sigma_{\rm g}^{\rm s0,e}}{\Sigma_{\rm g}^{\rm s0,s}}, \quad f_n \equiv \frac{n_{\rm e}}{n_{\rm s}}, \quad f_b \equiv \frac{b_{\rm e}}{b_{\rm s}}, \tag{23}$$

if f_Σ, f_n, and f_b are independent of m_r.

For instance, if we adopt $f_\Sigma = 0.1$ (Smith et al. 2012), $f_n = 0.6$ (Rowlands et al. 2012), and $f_b = 2$ (Skibba et al. 2009), we obtain $r = 0.77$. Thus our current result that $\Sigma^{\rm c0}_{\rm g,obs}(m_r)$ is smaller than $\Sigma^{\rm c0}_{\rm g,model}(m_r)$ may be, at least partly, accounted for by the morphological dependence of galaxies.

For reference, we repeat the above analysis by simply splitting the sample in two according to their $u-r$ color. Following Strateva et al. (2001), we adopt $u-r = 2.22$, to separate the galaxy types. The number fraction of these two galaxies types is $f_n = 2$, and the stacking analysis indicates $f_\Sigma = 0.2$. While the angular-correlation functions of the two types are not necessarily described the linear bias, we take the ratio at $\theta = 10'$ and find $f_b = 1.6$. These yields the value of integral ratio, $r = 0.84$. The morphology dependence does not seem to fully explain the possible discrepancy plotted in figure 14. This indicates that the discrepancy in figure 14 may be largely due to the extrapolation of magnitude dependence of angular-correlations to fainter magnitudes. In any case, the reliable conclusion can be reached only after the careful analysis in the many color bins.

6 Mean Dust Temperature of SDSS Galaxies

Another important advantage of AKARI FIS is its multi-band coverage. From the spectrum of the stacked FIR emission in different wavelengths, we can infer the mean dust temperature of SDSS galaxies. Kashiwagi & Suto (2015) proposed a method to constrain the dust extent through the measurement of dust temperature. They obtain constraints on the dust temperature by combining the far-infrared emission computed from the stacked images of the IRAS map with the quasar reddening measurement by Menard et al. (2010). The mean spectrum energy distribution of stacked SDSS galaxies is a more direct probe of the dust temperature and independent of the method proposed by Kashiwagi & Suto (2015).

We repeat the same stacking analysis over AKARI FIS maps at 65 and 140μm in addition to at 90μm as described in the previous sections. In particular, 140μm band is suited for the determination of the dust temperature because it is closer to the expected peak of the dust emission.

The best-fits of the amplitudes of the single term, $\Sigma_{\rm g}^{\rm s0}(m_r)$, at the different bands are translated to the fluxes $f(\nu_{\rm obs};m_r)$, and then fitted to the following grey-body spectrum:

$$f(\nu_{\rm obs};m_r)=D(m_r)\nu_{\rm obs}^{3+\beta}\left[\exp\left(\frac{h\nu_{\rm obs}}{k_{\rm B}T_{\rm dust,obs}}\right)-1\right]^{-1}. \tag{24}$$

We adopt the dust emissivity of $\beta=1.5$ for definiteness.

Figure 16 plots the spectral energy distribution (SED) of galaxies with $m_r=15.5$-16.0, 17.0-17.5, 18.5-19.0, and 20.0-20.5 in filled circles. The solid lines are their best-fits to equation (24), and fits are quite acceptable. The corresponding temperatures are $T_{\rm dust,obs}\approx 31$K for $m_r=15.5$-16.0, and $T_{\rm dust,obs}\approx 30$K for 17.0-17.5 to 20.0-20.5. It is also encouraging that the resulting temperature is almost independent of the magnitude as it should be.

Since the SDSS photometric galaxies are distributed over the range of redshifts, $T_{\rm dust,obs}$ is not identical to the mean of the dust temperature of the SDSS galaxies at different redshifts. If we assume all the SDSS galaxies are at their median redshift $\langle z\rangle$, the mean dust temperature at $\langle z\rangle$ is simply given by $T_{\rm dust,obs}(1+\langle z\rangle)$. This is not an accurate but reasonably good estimate for the redshift effect. If we adopt $\langle z\rangle=0.36$ (Dodelson et al. 2002), the dust temperature from our stacking analysis is close to 40K.

Note that we measured the dust temperature statistically, while the dust temperature of individually identified, thus IR luminous, galaxies are estimated with the Herschel Space Observatory (HSO) (Pilbratt et al. 2010). Our value is marginally consistent with 20-40K (e.g. Amblard et al. 2010, Hwang et al. 2010, Dunne et al. 2011, Hwang et al. 2011) which are estimated with the HSO.

Finally black open circles in figure 16 are the fluxes measured by KYS13 for IRAS. As mentioned in §4, the IRAS fluxes agree well with our AKARI result, while they are systematically underestimated for $m_r>18$. The consistent feature is clearly exhibited in figure 16.

7 Summary

In this paper, we present the image stacking analysis of the SDSS photometric galaxies over the AKARI Far-Infrared Surveyor maps at 65, 90, and 140μm. This enables us to identify the mean FIR counterparts of the SDSS galaxies down to the r-band magnitude of $m_r=20.5$ in a statistical fashion, corresponding to 3mJy at 90μm. A typical FIR flux of individually identified galaxies is about 10mJy. Therefore the image stacking analysis is useful in exploring the nature of typical galaxies in FIR that is not easily accessible otherwise. Our present result improves the previous analysis using IRAS at 100 μm by Kashiwagi, Yahata, & Suto. (2013) mainly thanks to a factor of 6 better angular resolution of AKARI (FWHM=53$''$ at 90μm) relative to IRAS (FWHM=6$'$ at 100μm).

We decompose the stacked image profiles of galaxies with different m_r into the single term and the clustering term. The single term represents the flux from the central galaxy, while the clustering term is a sum of contribution from near-by galaxies through their angular clustering. Because typical sizes of SDSS galaxies are much smaller than that of AKARI FIS PSF, the single term follows the PSF that is well approximated by the double Gaussians. The clustering term can be written in terms of the angular-correlation function that is directly measured from the SDSS galaxies in optical. Thus the FIR amplitude of the clustering term fitted from the stacked image profile can be compared with that predicted from the SDSS data.

This could be used in turn so as to explore the existence of the possible unknown class of optically faint and FIR luminous objects that are not traced by optical galaxies. Indeed Kashiwagi, Yahata, & Suto. (2013) suggested that the FIR fluxes inferred from IRAS data are not fully explained by the SDSS galaxies alone. Our present analysis, however, revealed that the extrapolation of the angular-correlation function of SDSS galaxies is sufficient to account for the detected FIR fluxes. In other words, the discrepancy does not require any additional class of objects, but can be explained by galaxies outside the SDSS magnitude range. This result may be interpreted as an example that the image stacking analysis can put useful constraints on the angular clustering of galaxies

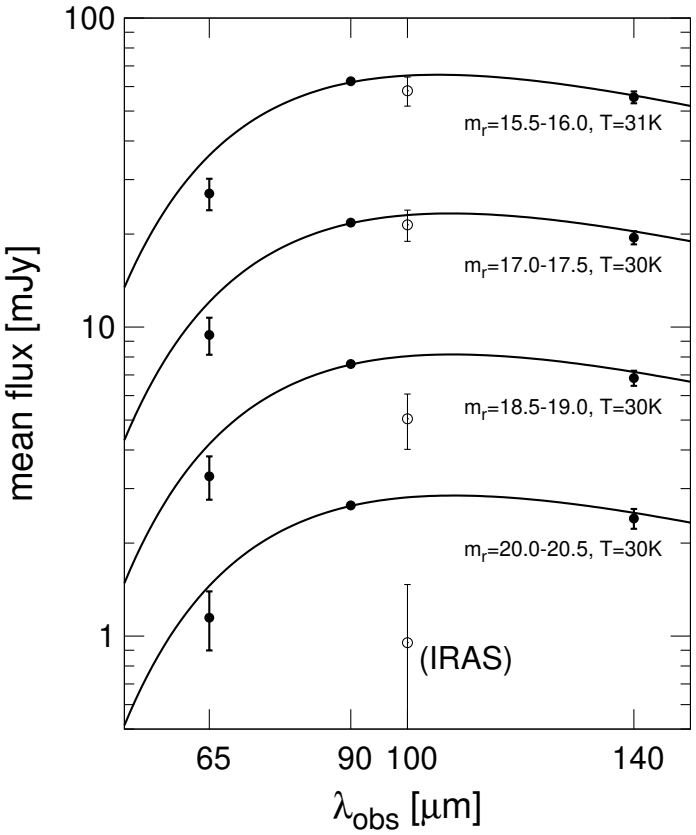

Fig. 16. The spectral energy distribution measured by FIS. Filled symbols and solid lines indicate the flux of single term measured by the stacking analysis (red filled symbols in figure(11)) and their best-fits of grey-body (eq.(24)), respectively. Their values of $m_r = 15.5$-16.0, 17.0-17.5, 18.5-19.0, and 20.0-20.5 correspond to symbols and lines from top to bottom. For reference, black open symbols plot the fluxes measured by the IRAS.

that are not easily probed otherwise.

We also combined the stacking analysis at 65μm, 90μm, and 140μm, and found that the mean dust temperature of the SDSS galaxies at $\langle z \rangle = 0.36$ is ~ 40K. This value is slightly higher than the typical dust temperature of galaxies that are FIR luminous and individually detected.

Our image stacking can be improved and applied for other purposes. First, the morphological dependence of the FIR emission of galaxies needs to be studied as mentioned in §5. Second, the analysis based on spectroscopic, rather than photometric, samples of galaxies is important in separating the redshift evolution and intrinsic luminosity dependence. Third, the current method can be applied to search for the intracluster dust that is not directly associated with individual galaxies, in a complementary fashion to Kashiwagi & Suto (2015) and Menard et al. (2010). Finally, it is interesting to perform the image stacking of quasars, as has been tentatively attempted by KYS13. We are currently working on those studies, and plan to present the result elsewhere.

Acknowledgements

We thank Masamune Oguri and Tetsu Kitayama for useful discussion. T.O. is supported by Advanced Leading Graduate Course for Photon Science (ALPS) at the University of Tokyo. T.K. gratefully acknowledges a support from Global Center for Excellence for Physical Science Frontier at the University of Tokyo. This work is supported in part from the Grant-in-Aid No. 20340041 by the Japan Society for the Promotion of Science. Data analysis was carried out on common use data analysis computer system at the Astronomy Data Center, ADC, of the National Astronomical Observatory of Japan.

This research is based on observations with AKARI, a JAXA project with the participation of ESA. Funding for the SDSS and SDSS-II has been provided by the Alfred P. Sloan Foundation, the Participating Institutions, the National Science Foundation, the U.S. Department of Energy, the National Aeronautics and Space Administration, the Japanese Monbukagakusho, the Max Planck

Society, and the Higher Education Funding Council for England. The SDSS Web Site is http://www.sdss.org/.

SDSS and SDSS-II are managed by the Astrophysical Research Consortium for the Participating Institutions. The Participating Institutions are the American Museum of Natural History, Astrophysical Institute Potsdam, University of Basel, Cambridge University, Case Western Reserve University, University of Chicago, Drexel University, Fermilab, the Institute for Advanced Study, the Japan Participation Group, Johns Hopkins University, the Joint Institute for Nuclear Astrophysics, the Kavli Institute for Particle Astrophysics and Cosmology, the Korean Scientist Group, the Chinese Academy of Sciences (LAMOST), Los Alamos National Laboratory, the Max-Planck-Institute for Astronomy (MPIA), the Max- Planck-Institute for Astrophysics (MPA), New Mexico State University, Ohio State University, University of Pittsburgh, University of Portsmouth, Princeton University, the United States Naval Observatory, and the University of Washington.

Appendix. Validity of the subtraction method of the foreground emission

In §4, we subtracted the foreground emission due to the Galactic dust, from the raw stacked images using the empirically constructed templates for the foregrounds. Although this method is successful in removing the foreground contribution fairly nicely, we carefully consider the extent to which the resulting best-fit parameters characterizing the FIR emission of galaxies, $\Sigma_{\rm g}^{\rm s0}(m_r)$ and $\Sigma_{\rm g}^{\rm c0}(m_r)$, are affected by this procedure.

For that purpose, we repeated the stacking analysis of the SDSS galaxies as presented in §3.2, but without subtracting any foreground contribution. We model the resulting radial profiles of galaxies as

$$\Sigma_{\rm g}^{\rm tot}(\boldsymbol{\theta};m_r)=\Sigma_{\rm g}^{\rm s}(\boldsymbol{\theta};m_r)+\Sigma_{\rm g}^{\rm c}(\boldsymbol{\theta};m_r)+C(m_r), \tag{25}$$

where $C(m_r)$ indicates the offset level due to the foreground emission. Here we treat $C(m_r)$ as a free parameter separately for each magnitude bin. We find that except that the statistical uncertainties become slightly smaller, the best-fit values of $\Sigma_{\rm g}^{\rm s0}(m_r)$ and $\Sigma_{\rm g}^{\rm c0}(m_r)$, are almost identical to from those derived without subtracting the foreground templates. Thus, the parameters characterizing the FIR emission of galaxies are very insensitive to how we subtract the foreground emission.

On the other hand, the best-fit parameter of $C(m_r)$ systematically decreases against m_r, as shown in figure 17, while the offset level due to the foreground emission is naively expected to be independent of m_r. The similar trend was also found by KYS13, using the IRAS data. KYS13 suggested that the unexpected correlation is due to the spatial inhomogeneities of the local universe, in particular, the CfA Great Wall (hereafter, CGW). They argued that the CGW is coincidentally located where the IRAS 100μm emission is relatively high. Since the nearby structure such as the CGW would consists of bright galaxies, the stacking results for the bright magnitude sample could return relatively large values of the Galactic foreground emission.

After the publication of KYS13, however, the authors found that this explanation is not likely to be correct, due to the over-interpretation of the results of the corresponding analysis; these results are rather subtle and should have been interpreted more carefully, especially since those statistical significances are limited by the number of the galaxies used in these analysis, which is much reduced by avoiding the CGW.

Indeed, the best-fit values of $C(m_r)$ for the AKARI results indicate the strong correlation with m_r, much beyond the quoted error-bars computed from the jackknife resampling. Given that the jackknife resampling method takes into account the sample variance over the survey area, the correlation should be interpreted to be present over the entire sky area, and would not be restricted to the specific region of the sky area, such as the CGW. Thus, the origin of the anomalous correlation needs to be further investigated in detail. We emphasize, however, that our results for the FIR emission of galaxies would not be affected by the value of those offset levels, as far as our assumption that the FIR emission of galaxies basically traces the spatial distribution of the optical galaxies.

References

Abazajian, K., et al. 2009, ApJS, 182, 543
Amblard, A., et al. 2010, A&A, 518, L9
Arimatsu, K., Doi, Y., Wada, T., Takita, S., Kawada, M., Matsuura, S., Ootsubo, T., & Kataza, H. 2014, PASJ, 66, 47
Cohen, M., Walker, R. G., Carter, B., Hammersley, P., Kidger, M., & Noguchi, K. 1999, AJ, 117, 1864
Connolly, A. J., et al. 2002, ApJ, 579, 42
Dodelson, S., et al. 2002, ApJ, 572, 140
Doi, Y., et al. 2015 PASJ, 67, 50
Dunne, L., et al. 2011, MNRAS, 417, 1510
Fukugita, M., Ichikawa, T., Gunn, J. E., Doi, M., Shimasaku, K. & Schneider, D. P. 1996, AJ, 111, 1748
Gorjina, V., Wright, E. L., & Chary, R. R. 2000 ApJ, 536, 550

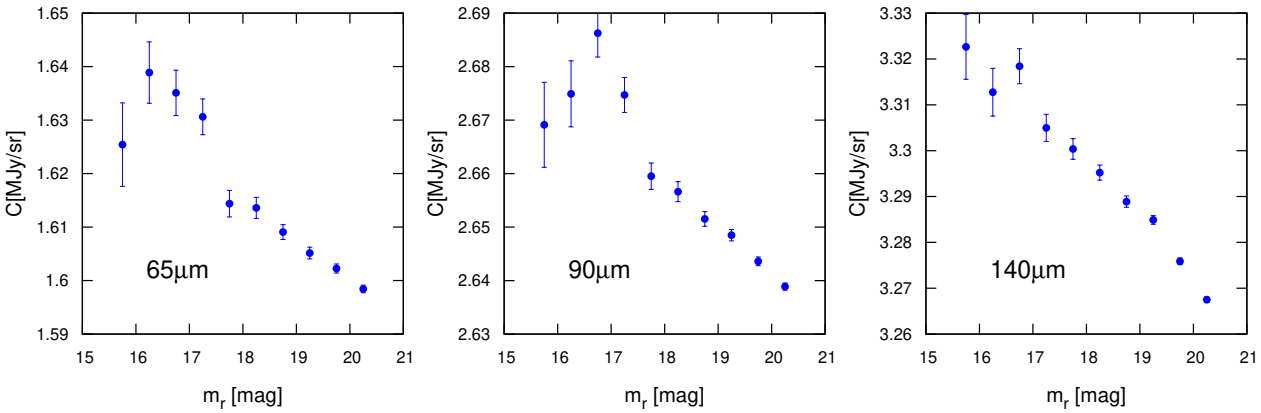

Fig. 17. The left, center, and right panels correspond to the best-fit parameters of constant term before removing the background at 65μm, 90μm, and 140μm, respectively.

Gunn, J. E., et al. 1998, AJ, 116, 3040
Gunn, J. E., et al. 2006, AJ, 131, 2332
Hogg, D. W., Finkbeiner, D. P., Schlegel, D. J. & Gunn, J. E. 2001, AJ, 122, 2129
Hwang, H. S., et al. 2010, MNRAS, 409, 75
Hwang, H. S., et al. 2011, A&A, 535, 60
Ivezić, Ž., et al. 2004, Astronomische Nachrichten, 325, 583
Kashiwagi, T., Yahata, K., & Suto, Y. 2013 PASJ, 65, 43 (KYS13)
Kashiwagi, T., Suto, Y., Taruya, A., Kayo, I., Nishimichi, T., & Yahata, K. 2015 ApJ, 799, 132
Kashiwagi, T., & Suto, Y. 2015 MNRAS, 451, 4162.
Kawada, M., et al. 2007, PASJ, 59, 389
Lutz, D. 2014, ARA&A, 52, 373
Matsuura, S., et al. 2011, ApJ, 737, 2
Menard, B., Scranton, R., Fukugita, M., & Richads, G. 2010, MNRAS, 405, 1025
Murakami, H., et al. 2007, PASJ, 59, 369
Padmanabhan, N., et al. 2008, ApJ, 674, 1217
Pier, J. R., Munn, J. A., Hindsley, R. B., Hennessy, G. S., Kent, S. M., Lupton, R. H., & Ivezić, Ž. 2003, AJ, 125, 1559
Pilbratt, G. L., et al. 2010, A&A, 518, L1
Rowlands, K., et al. 2012, MNRAS, 419, 2545
Schlegel, D., Finkbeiner, D., & Davis, M. 1998 AJ, 500, 525
Scranton, R., et al. 2002, ApJ, 579, 48
Skibba, R. A., et al. 2009, MNRAS, 399, 966
Smith, J. A., et al. 2002, AJ, 123, 2121
Smith, M.W.L., et al. 2012, ApJ, 748, 123
Stoughton, C., et al. 2002, AJ, 123, 485
Strateva, I., et al. 2001, AJ, 122, 1861
Takita, S. et al. 2015 PASJ, 67, 51
Tucker, D. L., et al. 2006, Astronomische Nachrichten, 327 821
Yahata, K., Yonehara, A., Suto, Y., Turner, E.L., Broadhurst, T., & Finkbeiner, D. 2007, PASJ, 59, 205
Yasuda, N., et al. 2001, AJ, 122, 1104
York, D. G., et al. 2000, AJ, 120, 1579